Journal of Alloys and Compounds 509S (2011) S46–S51

Contents lists available at ScienceDirect

Journal of Alloys and Compounds

journal homepage: www.elsevier.com/locate/jallcom

The crystallization behavior of amorphous Fe–Sn–B ribbons

Emília Illeková*, I. Mat'ko, P. Švec Sr., P. Švec, D. Janičkovič

Institute of Physics, Slovak Academy of Sciences, Dúbravska cesta 9, 845 11 Bratislava, Slovakia

ARTICLE INFO

Article history:
Received 2 July 2010
Received in revised form 8 December 2010
Accepted 9 December 2010
Available online 17 December 2010

Keywords:
Amorphous ribbons
Fe–B based
Fe–Sn–B
Curie point
DSC
Kinetics of crystallization

ABSTRACT

Amorphous $Fe_{(95-x)}Sn_5B_x$ ribbons ($x = 15, 17, 20$) were prepared for the first time by planar-flow casting. Their thermodynamic stability and kinetics of crystallization were studied by differential thermal analysis, differential scanning calorimetry and magnetometry (thermobalance with permanent magnet). Formation of crystalline phases and their morphology were analyzed by X-ray diffraction and transmission electron microscopy. The results indicate the existence of critical composition for the transformation kinetics. The relation between the magnetic state of the material and the kinetics of crystallization was analyzed.

1. Introduction

Fe–B based amorphous alloys due to their magnetic characteristics as well as being the most known principal foregoers for the nanocrystalline alloys have interesting application properties [1]. In addition, they are the pivotal soft magnetic metallic glasses which kinetics of crystallization, properties and influence of other elements have been widely inspected in hundreds of scientific papers as [2,3]. With respect to the elemental proportions in the as-quenched Fe–B based systems, the critical composition always exists and consequently different crystalline phases can grow in hypocritical and hypercritical alloys. Primary, polymorphous and eutectic types of crystallization have been observed forming traditionally spherulitic grains [4]. Recently also nanocrystallization has been referred for the Fe–B based ribbons as the consequence of either extreme heat-treatment or especial additives [5].

As Sn hardly dissolves in the solid Fe(Sn) and forms practically no solid solution with boron [6], the remaining solid inclusions of Sn are expected to prevent the amorphization of any Fe–Sn–B alloy. Probably for this reason only few results have been published on amorphous or rapidly quenched Fe–Sn–B ribbons [7] or on electroless amorphous alloy deposits [8] (in this case containing high content of Sn).

In this paper, the crystallization, magnetic phase transitions and melting of the Fe–Sn–B amorphous ribbons, especially $Fe_{78}Sb_5B_{17}$, are deeply studied and the role of Sn in the cited phenomena is investigated.

2. Experimental procedure

Three amorphous ribbons (6 mm wide and 30–45 μm thick), with the nominal composition of $Fe_{80}Sn_5B_{15}$, $Fe_{78}Sn_5B_{17}$ and $Fe_{75}Sn_5B_{20}$ (at %) were produced by planar flow casting from the temperature 1660 K at approximately 10^6 K s^{-1} in air. X-ray diffraction patterns were obtained by standard XRD using CuK_α radiation. In the as-cast ribbons of $Fe_{80}Sn_5B_{15}$ and $Fe_{78}Sn_5B_{17}$ no crystalline phases with observable grains were detected. The XRD detected weak lines of pure Sn in each as-cast $Fe_{75}Sn_5B_{20}$ ribbon. The morphology of the crystallized products was analyzed by transmission electron microscopy (TEM) using JEOL 2000 FX. Calorimetric signals from phase transformations were monitored by differential scanning calorimetry (DSC) using Perkin-Elmer DSC7 and high temperature differential thermal analysis (DTA) using Perkin-Elmer DTA7. Linear-heating regimes (at 9 heating rates, w, from 2 to 80 K min^{-1} for DSC and $w = 10$ K min^{-1} for DTA) and also the isothermal regime in the case of DSC (up to 900 min at 5 or 9 annealing temperatures, T_a, from 653 to 678 K and 698 to 743 K after the heating ramp at 40 K min^{-1}) for $Fe_{78}Sn_5B_{17}$ ribbon, and the flowing Ar atmosphere were used. Both instruments were calibrated, the error of established quantities is ±0.5 K and ±2 J g^{-1} for the DSC and ±2 K and ±4 J g^{-1} for the DTA for all heating rates. The thermomagnetometry measurements (TMG) were realized using the Perkin-Elmer TGA7 thermobalance with permanent magnet and linear-heating regime at $w = 2$, 10 and 40 K min^{-1} (±1.5 K and ±0.1 μg).

3. Results and discussion

Firstly, the appreciable structural relaxation of ~−10 J g^{-1}, starting below 470 K, reflects the virginity of all investigated ribbons. Heating at 40 K min^{-1}, the crystallization proceeds in two steps, R1 and R2 (Fig. 1), which have been characterized by the

* Corresponding author at: Department of Metals, Institute of Physics, Slovak Academy of Sciences, Dúbravska cesta 9, 845 11 Bratislava, Slovakia.
Tel.: +421 2 5941 0526; fax: +421 2 5477 6085.
E-mail address: fyziille@savba.sk (E. Illeková).

0925-8388/$ – see front matter © 2010 Elsevier B.V. All rights reserved.
doi:10.1016/j.jallcom.2010.12.063

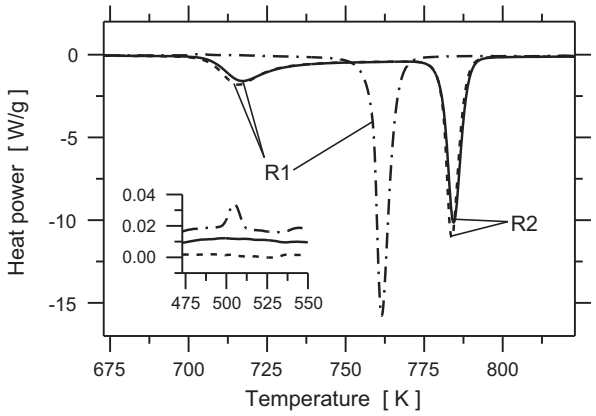

Fig. 1. DSC linear-heating curves from various as-prepared samples taken at 40 K min^{-1}. Dashed line – $Fe_{80}Sn_5B_{15}$, full line – $Fe_{78}Sn_5B_{17}$, and dash-and-dotted line – $Fe_{75}Sn_5B_{20}$. Crystallization steps R1 and R2 are identified. Eventual melting peak of pure Sn is seen in the inset.

onset temperatures, T_x, and crystallization enthalpies, ΔH, namely $T_{x1} = 705.5$ K, $\Delta H_1 = -70$ J g^{-1} and $T_{x2} = 780.5$ K, $\Delta H_2 = -91$ J g^{-1} for $Fe_{80}Sn_5B_{15}$ and similarly $T_{x1} = 706.5$ K, $\Delta H_1 = -64$ J g^{-1} and $T_{x2} = 780.5$ K, $\Delta H_2 = -92$ J g^{-1} for $Fe_{78}Sn_5B_{17}$ ribbon. Only one massive effect R1 with $T_{x1} = 758.5$ K, $\Delta H_1 = -151$ J g^{-1} has been identified in the case of $Fe_{75}Sn_5B_{20}$ ribbon (Fig. 1). According to the asymmetry in the kinetics of the continuous-heating crystallization effect [9], the DSC curves in Fig. 1 suggest nanocrystallization in the hypocritical $Fe_{(95-x)}Sn_5B_x$ alloys; however, the character of crystallization changes substantially towards the classical nucleation-and-growth (JMA) crystallization [9] when exceeding the critical composition (the binary eutectics for Fe and B is $Fe_{83}B_{17}$). Because the rate of crystallization strictly depends on temperature following the Arrhenius rule, crystallization peaks significantly shift to higher temperatures increasing the heating rate, as can be seen in Fig. 2. Nine heating rates have been used, the activation energies E^* of R1 and R2 crystallization steps have been determined by the use of the Kissinger method [10], namely $E_1^* = 289 \pm 4$ kJ mol^{-1}, $E_2^* = 346 \pm 5$ kJ mol^{-1} for $Fe_{80}Sn_5B_{15}$ and similarly $E_1^* = 296 \pm 3$ kJ mol^{-1}, $E_2^* = 327 \pm 2$ kJ mol^{-1} for $Fe_{78}Sn_5B_{17}$ ribbon. Surprisingly, similar value of $E_1^* = 289 \pm 7$ kJ mol^{-1} has been obtained also for $Fe_{75}Sn_5B_{20}$ ribbon. Though the Kissinger method was developed for the *n*th order reaction model, due to its simplicity and reproducible results it has been widely used also for the crystallization of metallic glasses considering E^* to be an apparent material parameter. Generally, results for E^* for the crystallization of Fe–B metallic glasses reported by several authors might differ appreciably mostly due to certain variability of the used thermoanalytical method, influence of structural relaxation and difference in population of quenched-in nuclei. The complex thermoanalytical approach of Illekovà et al. [11] gave reasons for the variance of ±16% for E_1^* and ±30% of E_2^* in the case of Fe–Si–B metallic glasses. In the simplest case, the most probable E^* for the crystallization of the $Fe_{80}B_{20}$ ribbon is $E^* = 241 \pm 5$ kJ mol^{-1} [12]. Decreasing the content of boron, E^* decreases down to 170 kJ mol^{-1} [13] and the crystallization splits into two steps. Smaller $E^* = 215$ kJ mol^{-1} has also been obtained for ternary $Fe_{75}Cr_5B_{20}$ ribbon [14] while substantial increase of both E_1^*~384–520 kJ mol^{-1} and E_2^*~372–459 kJ mol^{-1} has, for example, been reported for ternary Fe–Si–B alloys [3] or E_1^*~298–600 kJ mol^{-1} for the nanocrystallization in Fe–Cu–Nb–Si–B ribbons [15] or E_1^*~385–527 kJ mol^{-1} and E_2^*~408–502 kJ mol^{-1} for Fe–Mo–Cu–B ribbons [16]. The complexity of the crystallization in highly heterogeneous and anisotropic metallic ribbons is reflected also by the variation of both $E_1^*(T)$ and $E_2^*(T)$ with temperature [17] or decrease of $E_1^*(\alpha_1)$ in the advanced stages of R1 reaction (α_1 is the extent of conversion of the R1 reaction) in the case of hypo-critical Fe–Si–B ribbons [18] and also interrelation between $E_2^*(T_1)$ and the temperature of R1 crystallization step in the case of hyper-critical Fe–Si–B ribbons [11]. The behavior of E^*, being a parameter of an eventual kinetic model, of R1 and R2 crystallization steps for $Fe_{78}Sn_5B_{17}$ ribbon is analyzed in Fig. 3. The model-free Friedman–Gupta isoconversional method [19] and all continuous-heating DSC curves from Fig. 2 have been used. The results show that $E_1^*(\alpha_1)$, initially being constant, dramatically decreases for $\alpha_1 > 0.5$. $\alpha_1(T_{p1}) \sim 0.38$ for the temperature of the minimum of R1 peak (T_{p1}) independently of the heating rate reveals both the applicability of the Kissinger method and transience of the absolute value of E_1^* obtained. $E_2^*(\alpha_2)$ excepting $\alpha_2 < 0.15$ (reflecting the eventual superposition of R1 and R2 effects) and $\alpha_2 > 0.85$ (probably reflecting the uncertainty in the sigmoid baseline) is constant. $\alpha_2(T_{p2}) \sim 0.6$ designates the JMA kinetics. The quantity α_2 is the extent of conversion of the R2 reaction.

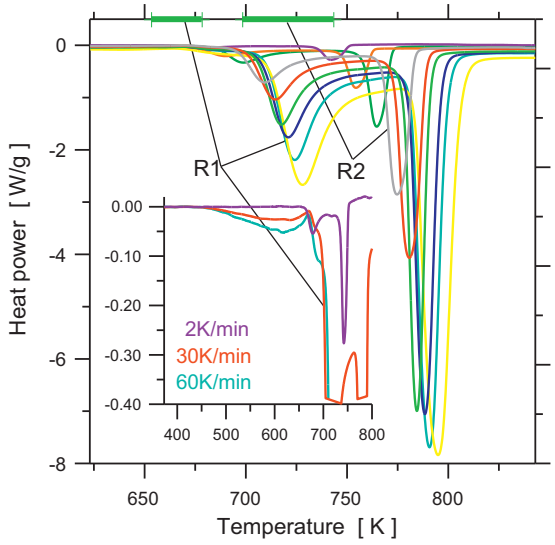

Fig. 2. DSC linear-heating curves for $Fe_{78}Sn_5B_{17}$ ribbon at 2, 5, 10, 20, 30, 40, 50, 60, 80 K min^{-1} (from left to the right). Intervals for isothermal experiments are highlighted in the upper *X*-axis. Curie point ($T_{c,a} = 671.5$ K at 40 K min^{-1}) is seen in the detail.

Moreover, the Curie temperature of the amorphous alloys ($T_{c,a} = 666.0$ K, 671.5 K or 714.0 K for $Fe_{80}Sn_5B_{15}$, $Fe_{78}Sn_5B_{17}$ or $Fe_{75}Sn_5B_{20}$ ribbon, respectively) being a minor effect in the DSC curve is closely preceding the crystallization. Contrariwise to the crystallization, the Curie effect being the second order phase transition does not depend on the heating rate. Thus, under certain heat-treatment, the crystallization might start at lower temperature $T_x < T_{c,a}$, as for example for $w = 2$ K min^{-1} being seen in the detail of Fig. 2. The relation between the magnetic Curie point and crystallization effect in the ribbons has been tested by the TMG measurements at various heating rates as in the case of DSC and they are presented in Fig. 4. In this case the major TMG effect is the drop of the magnetic mass at each T_c, while the formation of a new ferromagnetic phase due to the crystallization always evokes the increase in the TMG curve. The Curie temperatures determined by TMG ($T_{c,a} = 663$ K, 673 K or 712 K for $Fe_{80}Sn_5B_{15}$, $Fe_{78}Sn_5B_{17}$ or $Fe_{75}Sn_5B_{20}$ ribbon, respectively) coincide within the limits of errors with those predetermined by DSC. The consequent dualism (ferro/paramagnetism) in the eventual amorphous state within the R1 crystallization step might give the new reason for eventual variability in the effective kinetic parameters or the actual crystallization model.

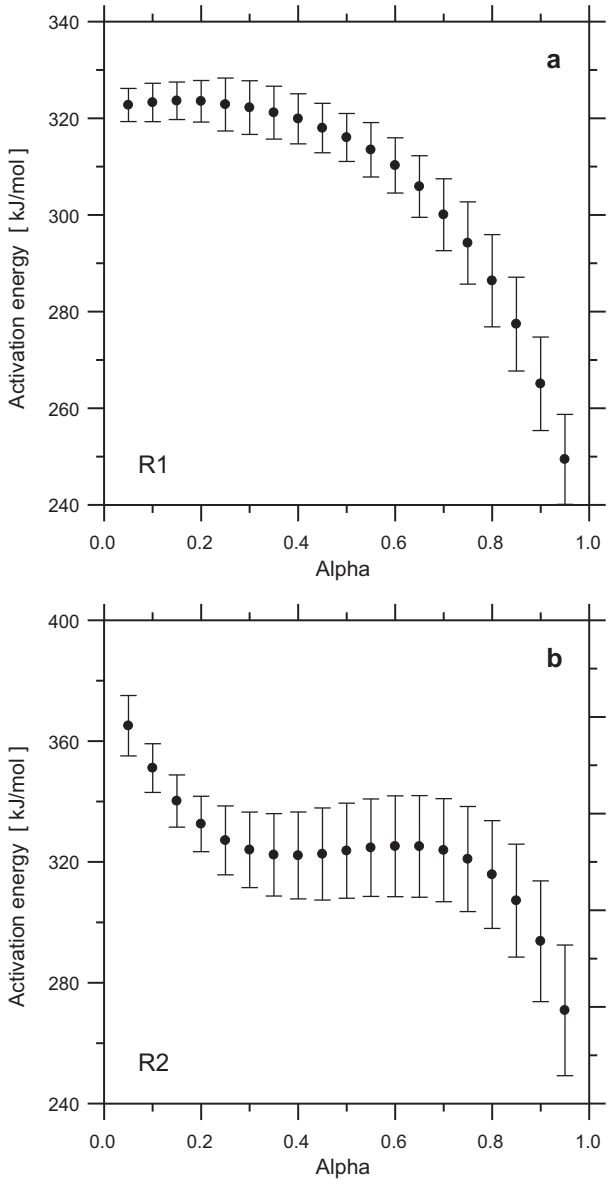

Fig. 3. Dependence of activation energy calculated by the isoconversional method on the extent of conversion for the continuous heating R1 (a) and R2 (b) crystallization steps of the as-quenched $Fe_{78}Sn_5B_{17}$ ribbon.

Recently, Paillier and Gebert [20] demonstrated that though the nucleation and growth should be the mechanisms of crystallization, the JMA-model need not to be applicable for example in the case of metallic glasses. It was also shown by Greer [2] that in spite of the complex character of the crystallization of rapidly quenched alloys, the simple JMA model is a good approximation in case of crystallization of $Fe_{80}B_{20}$ ribbons. Concerning Fe–Sn–B ribbons, the DSC signals show peaks for both crystallization steps also in the isothermal regime. The time of those peaks evidently depends on the annealing temperature, T_a, see Fig. 5, a fact which suggests the JMA kinetics [3]. It should be noted that to see complete isothermal exotherms in a DSC experiment, T_a has to be significantly lower than T_x. The relation between the real T_a, the actual $T_{c,a} = 671.5$ K and temperatures of linear-heating crystallization peaks for $Fe_{78}Sn_5B_{17}$ ribbon is marked in Fig. 2, too. Thus for $T_a > 671.5$ K, the R1 crystallization step takes part in the paramagnetic sample similarly as in the case of linear-heating, however, in the case of lower T_a, in its ferromagnetic predecessor.

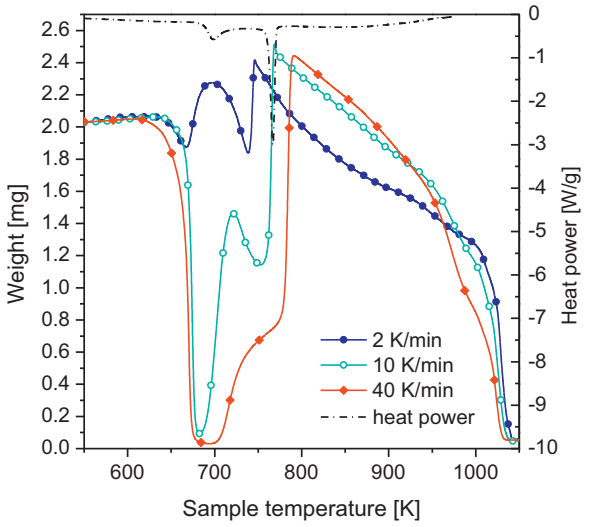

Fig. 4. TMG linear-heating curves from as-prepared $Fe_{78}Sn_5B_{17}$ samples taken at three heating rates; dashed-and-dotted line corresponds to the DSC curve for 10 K min^{-1}.

The competition between the JMA kinetics or the eventual normal-grain-growth kinetics (GG) distinguishing the classical metallic glasses from the precursors of the nanocrystalline alloys [9,21] has been tested by analyzing the experimental JMA exponent n or GG exponent m. The Suriñach curve fitting procedure [22] has been used. Fig. 6a shows, that all linear-heating curves from Fig. 2 unambiguously fit the JMA kinetics with $n_1 = 1.5$ if $\alpha < 0.25$ in the case of R1 crystallization step in $Fe_{78}Sn_5B_{17}$ ribbon. Later, the crystallization kinetics dramatically decays to $n_1 = 0.5$ or even the coalescence (GG kinetics with $m = 0.8$) might be reached. This result coincides with the $E_1^*(\alpha)$ dependence shown in Fig. 3. In the isothermal regime, however, the Suriñach representations of the DSC signals from inset of Fig. 5 change depending on the used T_a (see Fig. 6b). Thus if $T_a < T_{c,a}$, they fit well the JMA kinetics with $n_1 = 2$, as for $T_a = 668$ K. However, for $T_a > T_{c,a}$ if $\alpha < 0.35$ still $n_1 = 2$, then it gradually decreases down. This phenomenon – the difference in transformation kinetics at temperatures on both sides of the magnetic transition (Curie temperature), however, may also be

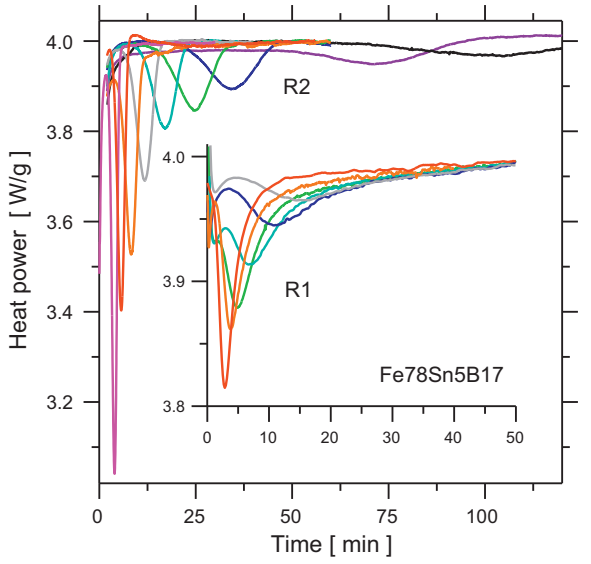

Fig. 5. DSC isothermal traces of $Fe_{78}Sn_5B_{17}$ ribbon for R2 crystallization step at $T_a = 743$, 738, 733, 728, 723, 718, 713, 703 and 698 K and for R1 crystallization step in the inset at $T_a = 678$, 673, 668, 663, 538 and 653 K (always from left to the right).

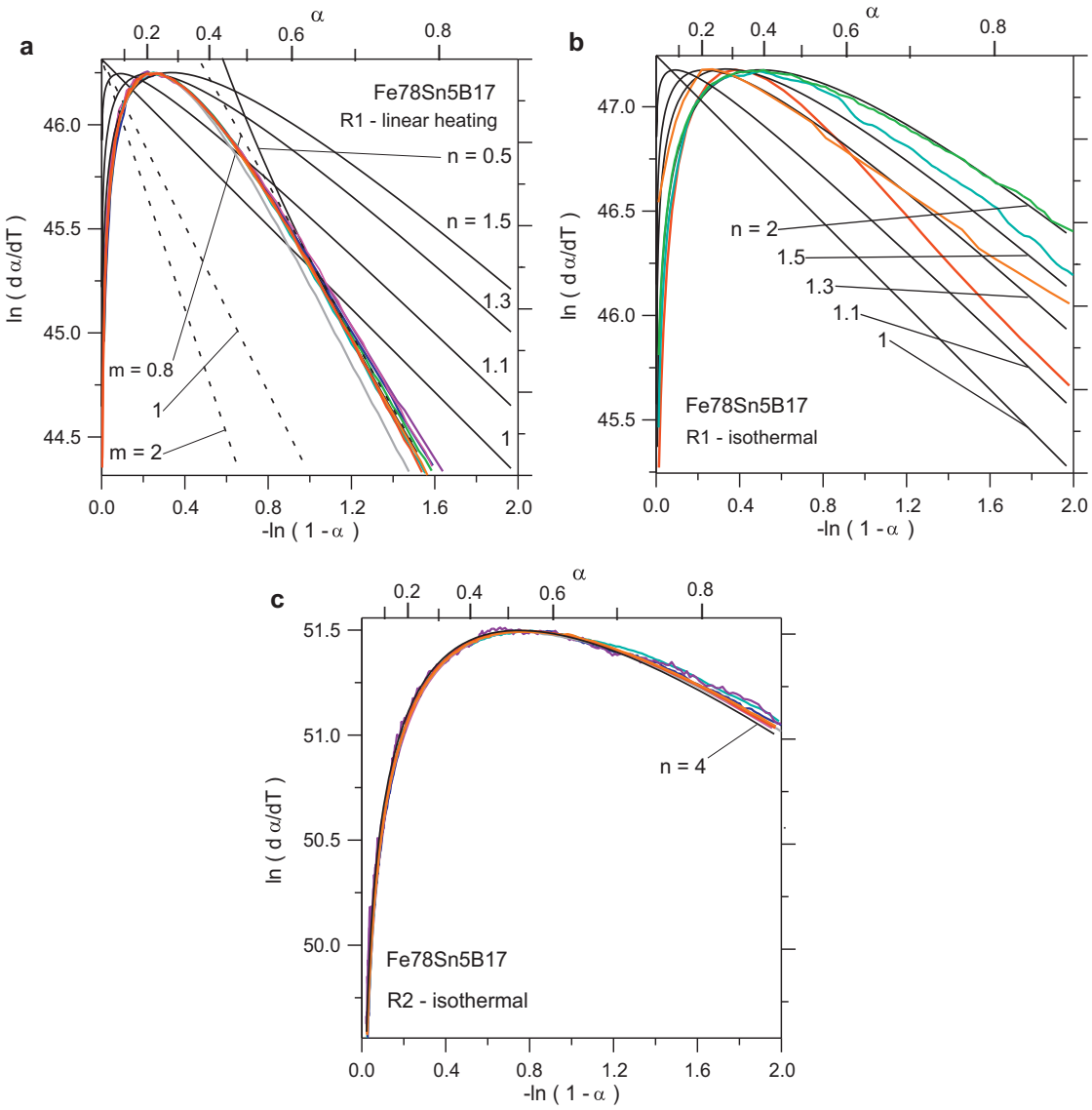

Fig. 6. Suriñach analyses for $Fe_{78}Sn_5B_{17}$ ribbon: (a) linear-heating regime, R1 crystallization step, (b) isothermal regime, R1 crystallization step, and (c) isothermal regime, R2 crystallization step. Colors of the curves are identical with colors of relevant DSC curves in Figs. 2 and 5. Full black lines – for JMA exponents $n = 4$, 2–1 or eventually 0.5. Dashed black lines – for NGG exponents $m = 2$, 1 or 0.8. The lines are the theoretical curves. The lines are vertically shifted to match with the experimental curves.

enhanced by the effect of temperature dependence of the kinetic parameters. In the case of R2 crystallization step, all isothermal curves from Fig. 5 coincide with the JMA kinetics and $n_2 = 4$ (see Fig. 6c).

Summarizing, the R1 and R2 kinetics are similar to those of Fe–Si–B glasses ($n_1 = 2.5$ and $n_2 = 4$, resp. 3 [3]) and simultaneously at the advanced stages, the R1 crystallization step suggests the FINEMET-like kinetics ($n_1 < 1$ or GG kinetics with $m_1 \sim 1$ [15]). The variation proceeds gradually. It should be related especially to the presence of Sn and to the magnetic state of the amorphous structure.

The XRD patterns confirm the amorphous state of $Fe_{80}Sn_5B_{15}$ and $Fe_{78}Sn_5B_{17}$ as-quenched ribbons (curve 3 in Fig. 7). In the case of $Fe_{75}Sn_5B_{20}$, narrow Sn lines in the amorphous halo clearly identify the presence of Sn on the air side of the ribbon (curve 2 in Fig. 7). The presence of pure Sn, however, has been detected only at the air surface of the ribbon; no traces of this element were obtained on the wheel side of the sample (curve 1 in Fig. 7; diffraction peaks of Sn significantly decreased in intensity are detectable in this diffraction pattern only due to air pockets). Both hypocritical compositions crystallize in a similar manner. For $Fe_{78}Sn_5B_{17}$ after annealing at 673 K (the region of R1 peak, curve 4 in Fig. 7), the formation of bcc-Fe(Sn) phase takes place. At higher temperatures (above 723 K, curve 5 in Fig. 7), the formation of Fe_2B takes place from the remaining amorphous matrix and the supersaturation of bcc-Fe(Sn) with Sn decreases, as indicated by a decrease of the bcc-Fe(Sn) lattice parameter from 0.2903 ± 0.00005 nm at 723 K down to 0.28866 ± 0.00005 nm at 873 K [23]. Atoms of Sn are probably accommodated also in the in Fe_2B, which is in accord with the observations in [24].

The TEM image of advanced stage of R1 crystallization step (673 K for 30 min) of $Fe_{78}Sn_5B_{17}$ is shown in Fig. 8. Crystalline grains of bcc-Fe(Sn) of equiaxed morphology and size up to ~50 nm are embedded in remaining amorphous matrix. The size distribution of the grains and the simultaneous presence of tiny as well as well developed particles are in accord with the notion of nucleation and growth mechanism taking place in this reaction step. The grains are significantly smaller than in the case of binary Fe–B glasses and their population is quite high. The presence of Sn thus probably leads to intensified nucleation while grain growth decays rapidly with annealing time (or proceeding reaction), causing the termination of the R1 JMA-like crystallization stage.

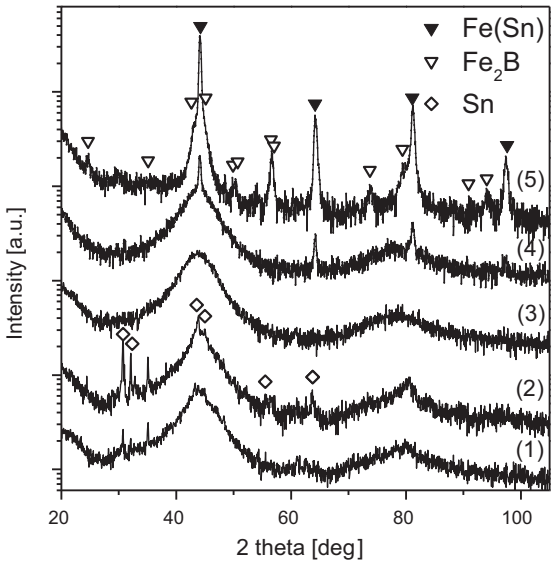

Fig. 7. XRD diffraction patterns of $Fe_{78}Sn_5B_{17}$ and $Fe_{75}Sn_5B_{20}$ ribbons. Patterns (1) and (2) as-quenched state of wheel and air side of $Fe_{75}Sn_5B_{20}$, respectively, (3) as-quenched state of top side of $Fe_{78}Sn_5B_{17}$ ribbon, (4) after isothermal annealing at 673 K for 30 min (the R1 step), and (5) at 723K for 30 min (the R2 step).

The melting of our samples is reversible and it consists of three events, M1, M2 and M3, as can be seen in the DTA curves in Fig. 9. Consistently with the results of the XRD its interpretation is the following. In the case of $Fe_{80}Sn_5B_{15}$ and $Fe_{78}Sn_5B_{17}$ alloys, the melting proceeds in the same way. The M2 effect (T_{x2} = 1395 K, ΔH_2 = 192 or, eventually, 167 J g^{-1}) represents the melting of the Fe(Sn) + Fe_2B eutectics (T_m = 1447 K in the binary Fe–B phase diagram [6]). Then the melting is finalized in the shallow endotherm M3 the end temperature of which (T_{e3} = 1471 K, or, eventually, 1463 K) is the liquidus and it reflects the actual compositions. In the case of $Fe_{75}Sn_5B_{20}$ alloy, the smaller and more curved peak M2 (T_x = 1380 K, ΔH_2 = 96 J g^{-1}) belongs (also) to the monotectic melting of Sn and Fe(Sn) (T_m = 1403 K in the binary phase diagram [6]). Therefore, the relevant liquidus is at significantly higher temperature, T_{e3} = 1567 K. The first melting peak M1 (T_{x1} = 1359 K, ΔH_1 = 10, 12, or 29 J g^{-1}) looks the same for all three samples, being significantly bigger for $Fe_{75}Sn_5B_{20}$. We did not find any equilibrium phase transition in the respective binary phase diagrams and thus its interpretation is still open.

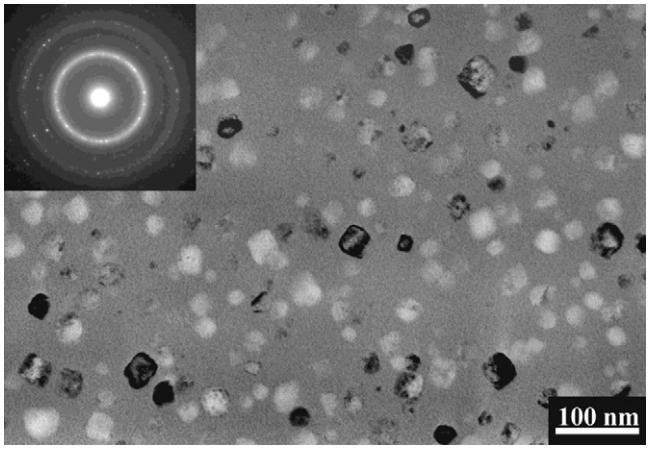

Fig. 8. The TEM image of advanced stage of R1 crystallization step (673 K for 30 min) of $Fe_{78}Sn_5B_{17}$ ribbon. Corresponding electron diffraction pattern (inset) contains besides diffuse hallo coming from remaining amorphous matrix only lines bcc-Fe(Sn) structure.

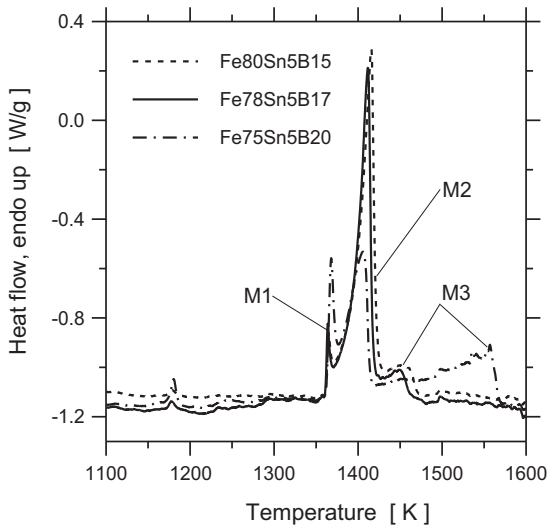

Fig. 9. DTA linear-heating curves from various as-prepared samples taken at 40 K min^{-1}. Dashed line – $Fe_{80}Sn_5B_{15}$, full line – $Fe_{78}Sn_5B_{17}$, and dash-and-dotted line – $Fe_{75}Sn_5B_{20}$. Melting steps M1, M2 and M3 are identified.

4. Conclusions

The aim of the present study was to analyze the peculiarities connected with the glass-forming ability and particular character of the crystallization of amorphous Fe–Sn–B ribbons:

1. Increasing the content of B at the expense of Fe the dissolution ability of Sn (in Fe) decreases. The remaining elemental Sn inhibits the glass-forming ability of Fe–Sn–B alloy.
2. With respect to mutual proportions of Fe and Sn, Fe–Sn_5–B ribbons belong to hypocritical ($Fe_{80}Sn_5B_{15}$, $Fe_{78}Sn_5B_{17}$) and hypercritical ($Fe_{75}Sn_5B_{20}$) systems.
3. Crystallization of $Fe_{78}Sn_5B_{17}$ is controlled by the JMA kinetics, however, due to the presence of Sn the nucleation is very intense and growth of the grains rapidly decays.
4. Crystallization kinetics of $Fe_{78}Sn_5B_{17}$ in paramagnetic and ferromagnetic states is not the same. Increasing temperature above $T_{c,a}$, either isothermally (at T_a > 671.5 K) or by linear-heating (for all w), the kinetics of R1 crystallization step (both activation energy and exponent) rapidly decreases.

Acknowledgements

Support of the Agency of the Ministry of Education of the Slovak Republic for the Structural Funds of the EU (CEKOMAT I, ITMS 26240120006) is gratefully acknowledged. The research was supported also by the projects VEGA 2/0157/08, APVV-0102-07 and by the CEX SAS "NANOSMART".

References

[1] Y. Yoshizawa, S. Oguma, K. Yamaguchi, J. Appl. Phys. 64 (1988) 6044.
[2] A.L. Greer, Acta Metall. 30 (1982) 171.
[3] I. Mat'ko, E. Illeková, P. Švec, P. Duhaj, Mater. Sci. Eng. A225 (1997) 145.
[4] U. Köster, in: B.L. Mordike (Ed.), Phase Transformations in Crystalline and Amorphous Alloys, DGM, Oberursel, 1983, p. 113.
[5] P. Svec, I. Janotova, G. Vlasak, D. Janickovic, J. Marcin, J. Kovac, I. Skorvanek, P. Svec Sr., IEEE Trans. Magn. 46 (2010) 408.
[6] H. Okamoto, Phase Diagrams of Binary Iron Alloys, ASM International, Materials Park, 1993, pp. 131–137.
[7] R.A. Dunlap, Solid State Commun. 43 (1982) 57.
[8] L. Wang, L. Zhao, B. Zhang, W. Hu, X. Shu, X. Sheng, Z. Fang, J. Alloys Compd. 287 (1999) 234.
[9] E. Illeková, K. Czomorová, F.A. Kuhnast, J.M. Fiorani, Mater. Sci. Eng. A205 (1996) 166.
[10] H.E. Kissinger, Anal. Chem. 29 (1957) 1702.

[11] E. Illeková, I. Mat'ko, P. Duhaj, F.A. Kunast, J. Mater. Sci. 32 (1997) 4645.
[12] J.A. Leake, A.L. Greer, J. Non-Cryst. Solids 38–39 (1980) 735.
[13] F.E. Luborsky, H.H. Lieberman, Appl. Phys. Lett. 33 (1978) 233.
[14] I. Mihalca, A. Ercuta, I. Zaharie, V. Kuncser, G. Filoti, A. Jianu, J. Optoelectron. Adv. Mater 3 (2001) 141.
[15] E. Illeková, Thermochim. Acta 387 (2002) 47.
[16] E. Illeková, D. Janičkovič, M. Miglierini, I. Škorvánek, P. Švec, JMMM 304 (2006) e636.
[17] E. Illeková, Thermochim. Acta 280/281 (1996) 289.
[18] E. Illeková, F. Malizia, F. Ronkoni, Thermochim. Acta 282/283 (1996) 91.
[19] M.J. Starink, Thermochim. Acta 404 (2003) 163.
[20] J. Paillier, A. Gebert, Thermochim. Acta 497 (2010) 85.
[21] E. Illeková, in: B. Idzikowski, P. Švec, M. Miglierini (Eds.), Properties and Applications of Nanocrystalline Alloys from Amorphous Precursors, NATO Science Series II: Mathematics, Physics and Chemistry, vol. 184, Kluwer Academic Publishers, Dordrecht, 2005, p. 79.
[22] S. Suriñach, M.D. Baró, M.T. Calvaguera-Mora, N. Clavaguera, J. Non-Cryst. Solids 58 (1983) 209.
[23] H. Okamoto, Phase Diagrams of Binary Iron Alloys, ASM International, Materials Park, 1993, p. 385.
[24] M. Miglierini, V.S. Rusakov, AIP Conf. Proc., vol. 1258, Melville, NY, 2010, p. 29.